Electrochimica Acta 273 (2018) 80–87

Contents lists available at ScienceDirect

Electrochimica Acta

journal homepage: www.elsevier.com/locate/electacta

Polymer-assisted chemical solution synthesis of $La_{0.8}Sr_{0.2}MnO_3$-based perovskite with A-site deficiency and cobalt-doping for bifunctional oxygen catalyst in alkaline media

Weichuan Xu, Litao Yan, Lara Teich, Steven Liaw, Meng Zhou**, Hongmei Luo*

Department of Chemical and Materials Engineering, New Mexico State University, New Mexico 88003, United States

ARTICLE INFO

Article history:
Received 26 January 2018
Received in revised form
22 March 2018
Accepted 6 April 2018
Available online 7 April 2018

Keywords:
Bifunctional perovskite catalyst
B-site cation doping
A-site deficiency
Low total overpotential
Network

ABSTRACT

The polymer-assisted chemical solution (PACS) method was used for the synthesis of $La_{0.8}Sr_{0.2}MnO_3$ (LSM)-based perovskite catalyst network with nanoparticle size of 30–80 nm to enhance oxygen evolution reaction (OER) activity and maintain highly active oxygen reduction reaction (ORR). Samples investigated include the A-site cation deficient $(La_{0.8}Sr_{0.2})_{0.95}MnO_{3-\delta}$ (ALSM) and the A-site cation deficient with the B-site cobalt-doped $(La_{0.8}Sr_{0.2})_{1-x}Mn_{1-x}Co_xO_{3-\delta}$ (x = 0.05 and 0.1 for LSMC5 and LSMC10, respectively). X-ray diffraction (XRD), transmission electron microscopy (TEM), and X-ray photoelectron spectroscopy (XPS) aided in physical characterizations. Electrochemical properties were tested in 0.1 M KOH solution by cyclic voltammetry (CV), linear sweep voltammetry (LSV) and electrochemical impedance spectroscopy (EIS). Our results indicate as compared to LSM, the lattice-shrunk ALSM with high oxygen vacancy displays enhanced OER performance, but its inferior ORR activity could be caused by reduced crystallinity. LSMC5 and LSMC10 show lowest total overpotential (0.93 and 0.91 V *vs.* Ag/AgCl (3.5 M)) with slightly less efficient ORR, despite their superior specific kinetic current density. Oxygen vacancy induces Fermi level upshift and reduced resistivity, while Co-doping increases orbital hybridization and enhances charge transfer. Understanding how the A-site non-stoichiometry and the B-site doping influence the B–O covalence is the key to the rational design of perovskite bifunctional oxygen catalysts.

1. Introduction

Increasing demand for clean and renewable energy necessitates less air pollutants from energy devices at both the industrial and household levels. Oxygen Reduction Reaction (ORR) and Oxygen Evolution Reaction (OER) used in fuel cells [1,2], metal-air batteries [3,4], and electrolyzer [5,6] have no waste regarding operation and recycling, as compared to conventional energy storage devices. However, environment benignity comes at the cost of sluggish reaction kinetics of oxygen involved reactions [7,8], and thus these are the rate limiting reactions and the bottleneck of maximum device power. Furthermore, catalysts with highest reported ORR and OER abilities are noble metals and noble metal oxides with prohibitive cost. Platinum, as a highly active ORR catalyst, unfortunately exhibits unsatisfying OER catalytic ability due to the surface platinum oxide formation in alkaline media at high potentials [9]. Ruthenium and iridium-based precious metal oxides are OER gold standard in acidic media, notwithstanding the 300–400 mV overpotentials [10] and ineffective ORR [9]. Considering the high expense and the scarcity of noble metals alongside the need for unitized reversible fuel cell/electrolyzer and metal-air batteries, tremendous efforts toward the design of alternative bifunctional catalyst from abundant and low-cost sources have been made, such as metal-nitrogen complexes [11,12], metal chalcogenides [13,14], carbonaceous compounds [15–17], and perovskite oxides [18–20]. Also, novel materials with materials defect such as layered double hydroxide nanosheets [21–23] and 3D carbon electrocatalysts [24] are showing new direction for OER/ORR electrocatalysis.

Perovskite oxide family with the formula of ABO_3, where A is a rare-earth metal or alkaline metal and B is a transition metal, has been identified as a bifunctional catalyst for ORR and OER. The active B-site cation on which the adsorption and desorption of

* Corresponding author.
** Corresponding author.
E-mail addresses: mzhou@nmsu.edu (M. Zhou), hluo@nmsu.edu (H. Luo).

https://doi.org/10.1016/j.electacta.2018.04.046
0013-4686/

oxygenated species occur has a six-fold corner-sharing octahedral symmetry with oxygen ligands. The five 3 d orbitals of the transition metal hybridized with 2*p* orbitals from oxygen split in this crystal field and become two degenerate e_g orbitals and three degenerate t_{2g} orbitals, both carrying 3 d and 2*p* features. The number of electrons filling in the e_g orbital directly influences the ORR and OER activity as the electron can form σ-bond with the adsorbates. Common catalytic ability improving modifications include the A-site deficiency, the A-site doping and the B-site doping methods. To tune the electronic structure of the perovskite lattice, one can change the content of surface oxygen vacancy, and further tweak the B–O bond strength or the B-site cation covalence.

$La_{0.8}Sr_{0.2}MnO_3$ as a A-site doped perovskite oxide catalyst has been confirmed for enhanced ORR performance in $La_{1-x}Sr_xMnO_3$ (x = 0–0.4) series [25]. According to the charge equilibrium theory, when introducing Sr^{2+} into the La^{3+} site, small amounts of Mn^{3+} cations will share one more electron with surrounding oxygen and become Mn^{4+}. In $La_{0.8}Sr_{0.2}MnO_3$, Mn cation has an average oxidation state of $Mn^{+3.2}$, and the *d*-shell electron configuration changes to $t_{2g}^3e_g^{0.8}$ with the hypothesis of Mn cations in high spin state, considering that the crystal field of O^{2-} is relatively weak. Shao Horn's theory [26] predicts high ORR efficiency with the e_g orbital occupancy close to but slightly less than unity, which explains the increased ORR activity of Sr-doped $LaMnO_3$ perovskite oxide. Nevertheless, insufficient number of e_g electrons in Mn based perovskite translates to inferior OER performance as the catalyst requires high overpotential to deprotonate oxyhydroxide groups, thus our goal is to tune electronic structure of $La_{0.8}Sr_{0.2}MnO_3$ to achieve enhanced OER catalytic ability and maintain high ORR activity.

By decreasing the A-site metal ion concentration, a perovskite oxide lattice with both the A-site deficiency and surface oxygen vacancy can be produced [27]. Positively charged surface oxygen vacancy attracts OH^- ions in alkaline media, and the higher covalence between the B-site cation and oxygen benefits charge transfer from the catalyst surface to adsorbates [26]; both characteristics are ideal for OER. Introducing the B-site doping is another effective method of changing physical and chemical properties of perovskite oxides. Doping brings inequality of electron/hole carriers and increases the free carrier concentration. The doped B-site metal B′ has an impact on catalytic activity by tuning the host B-site metal oxidation state, i.e. the outer shell electron configuration, and the current contribution from the new $B'O_6$ structure. In search of alternative B-site cations, Co is of special interest as its charge states results in e_g occupation between 1 and 2, and therefore strong OER ability in perovskite catalysts [28]. We combine the features above in an attempt to enhance OER performance in Mn based perovskite to achieve catalyst bifunctionality.

Since most perovskite oxide preparation methods involve sol-gel technique [27,29,30] followed by high temperature annealing (>1000 °C) [29,31], it is not surprising to find agglomeration of particles with μm scales [27]. Samples of such particle sizes usually need carbon addition during catalyst ink preparation to eliminate charge transfer limitation. Here we introduce a facile polymer-assisted chemical solution (PACS) method for the synthesis of $La_{0.8}Sr_{0.2}MnO_3$-based perovskites at 650 °C. Adapted from Polymer-assisted deposition (PAD) method that has been used for crack-free epitaxial thin film synthesis in photocatalysis application [32,33], PACS further extends the scope to powder catalyst preparation for biocatalysis [34], catalytic combustion [35] and electrochemical catalysis [36]. Metal cations can bind to poly(ethylenimine) (PEI) and ethylenediaminetetraacetic acid (EDTA), and the polymers bind to each other through hydrogen bonding and electrostatic attraction [37] to avoid cations pre-mature precipitation. Samples one-step synthesized with this method have nanoparticle size <100 nm. Catalyst support materials feature high surface area originating from medium temperature process. Our perovskite catalyst showed nanoparticle size around 30–80 nm and enhanced ORR and OER catalytic performance including one of the lowest total overpotential in alkaline solution.

2. Experimental section

2.1. Synthesis of LSM

For $La_{0.8}Sr_{0.2}MnO_3$ (LSM) synthesis, 2 g poly(ethylenimine) (PEI) solution (Sigma-Aldrich, 50% w/v in H_2O), 1 g ethylenediaminetetraacetic acid (EDTA) (Sigma-Aldrich, >99.4%), and 10 mL H_2O were mixed and stirred in a beaker. Additionally, 0.35 g $La(NO_3)_3\cdot 6H_2O$ (Sigma-Aldrich, 99.99%), 0.042 g $Sr(NO_3)_2$ (Sigma-Aldrich, 99.995%), and 0.25 g $(CH_3COO)_2Mn\cdot 4H_2O$ (Aldrich, >99%) were added into the polymer solution. After further stirring, the solution was transferred into a crucible. The precursors were heated at 150 °C for 1 h with a heating rate of 1 °C/min to remove water, then heated at 650 °C for 3 h.

2.2. Synthesis of ALSM, LSMC5 and LSMC10

The A-site deficient $(La_{0.8}Sr_{0.2})_{0.95}MnO_{3-\delta}$ and samples with both the A-site deficiency and B-site doping $(La_{0.8}Sr_{0.2})_{1-x}Mn_{1-x}Co_xO_{3-\delta}$ (x = 0.05 and 0.10) were prepared with the same method, with $Co(NO_3)_2\cdot 6H_2O$ (Sigma-Aldrich, 99.999%) as cobalt precursor. Phase separation was reported when A-site deficiency reaches 20% in $La_{1-x}FeO_3$ [27], therefore we kept x value below 10%.

2.3. Materials characterization

The crystalline phases of $La_{0.8}Sr_{0.2}MnO_3$-based samples were investigated with X-ray diffraction (XRD) on a EMPYREAN SERIES 2, PANalytical, using filtered Cu Kα radiation (λ = 1.5405980 Å) at 45 kV and 40 mA. The morphology and particle size were analyzed with transmission electron microscopy (TEM) on H-7650, Hitachi High-Technologies Corp. The test used an accelerating voltage at 80 kV, filament voltage at 21 V, and beam current at 35 μA. Crystalline structure of LSM was further observed by high-resolution transmission electron microscopy (HRTEM) and selected area electron diffraction (SAED) on a JEOL, model JEM- 2100 operated at 200 kV. The surface chemistry was studied by X-ray photoelectron spectroscopy (XPS) on Thermo K-Alpha spectrometer equipped with a monochromatic Al kα X-ray source.

2.4. Electrochemical characterization

A glassy carbon rotating-disk electrode (RDE) was polished with 5, 0.3, and 0.05 μm Al_2O_3 solution (Allied) in sequence, for 5 min per solution. The electrode was then cleaned with H_2O and dried with compressed air. Catalyst ink was prepared by dissolving 5 mg oxide powder in 1 mL H_2O with 0.05 wt% diluted Nafion® 117 solution (Sigma-Aldrich). Contrary to many other works, no conductive carbon was added to eliminate the resistivity limitation. After sonication, an aliquot of 10 μL catalyst ink was cast dropwise on the glassy carbon electrode of 0.196 cm^2 area with a micropipette. The electrode was dried at 50 °C for 15 min. Electrochemical tests were performed on a MSR Rotator, PINE research and CH Instrument 760C electrochemical potentiostat. Three electrodes setup was implemented at room temperature: a working electrode, a Pt coil counter electrode and a silver chloride Ag/AgCl (3.5 M) reference electrode.

All electrochemical measurement data were iR corrected with the $E = E_0$ - iR equation, where E_0 is the recorded potential, i is the

recorded current, and R is the compensated electro-impedance (~49 Ω) in 0.1 M KOH solution.

ORR kinetics was evaluated with Koutecký - Levich analysis. Measured current density J consists of kinetic current density J_K and oxygen diffusion limited current density J_D. The equation for RDE is shown below:

$$\frac{1}{J}=\frac{1}{J_K}+\frac{1}{J_D}=\frac{1}{J_K}+M\frac{1}{n}\frac{1}{\omega^{1/2}} \quad (1)$$

where $M = 1/[0.62FAC_{O2}D_{O2}^{2/3}v^{-1/6}]$. F is Faraday constant (C mol^{-1}), A is electrode area (cm^2), C_{O2} is O_2 concentration in alkaline solution (mol cm^{-3}), D_{O2} is O_2 diffusion coefficient in 0.1 M KOH (cm^2 s^{-1}), v is viscosity of solution (cm^2 s^{-1}), n is electron transfer number and ω is angular rotation rate of the electrode (rad s^{-1}).

3. Results and discussion

All samples were characterized by XRD and showed single phase rhombohedral lattice in trigonal crystal system with space group of R-3c:R(167) [38]. The sample peaks are well indexed by PDF 01-075-3215. The ALSM with 5% A-site deficiency affords reduced crystallinity as compared to LSM, whilst Co doping facilitates crystallization as shown in Fig. 1a. In Fig. 1b regional XRD on (024) plane of ALSM, LSMC5 and LSMC10 demonstrates peak shifting to different directions. ALSM has positively shifted peak indicating the lattice shrinkage that can be attributed to the A-site deficiency and oxygen vacancy to preserve charge equilibrium. Interestingly, LSMC5 has negatively shifted peaks relative to ALSM. Since LSMC5 is expected to have similar A-site deficiency content as ALSM, the peak shifting and the increased lattice parameters could be ascribed to the larger Co (+2, +3) ionic radius compared with that of Mn (+3, +4). The shifting trend is more notable for LSMC10, and this observation is in agreement with the Vegard's law. Lattice parameters based on hexagonal metric and the size of crystallite calculated with Scherrer's Equation are tabulated in Table 1.

Morphology and particle size of samples were investigated by transmission electron microscopy. TEM images of $La_{0.8}Sr_{0.2}MnO_3$-based perovskite oxides are shown in Fig. 2. All images show overall inter-connected double- or triple-layer particles with size around 30–80 nm, which is consistent with the XRD result. Particles of irregular shapes were observed in all samples. Compared to perovskite oxides of micrometer scale from sol-gel method or EDTA-citrate acid precipitation method [27], the relatively uniform size distribution without severe coalesce in our perovskites stems from the unique metal-polymer solution chemistry, as the polymers bind with metal ions to prevent metal from hydrolysis or condensation [39]. Also, relatively low heating temperature of 650 °C is another key factor that can avoid particle aggregation. In Fig. 2e, connected LSM nanoparticles extend to several micrometers across the network, enabling fast electron or charge transfer between catalyst particles.

Table 1
Lattice parameters with hexagonal metric and crystallite size by Scherrer's Equation.

Samples	a (Å)	c (Å)	Crystallite size (nm)
LSM	5.5091	13.3211	25
ALSM	5.4992	13.2971	24
LSMC5	5.5070	13.3158	27
LSMC10	5.5249	13.3591	21

HRTEM and SAED were conducted on LSM to further study the crystalline phase and microstructure of perovskite oxide with the PACS method. Fig. 3a shows multiple lattice periodical arrangement with interplanar spacing of (021) and (110) planes calculated as $d_{(021)} = 0.3884$ nm and $d_{(110)} = 0.2761$ nm, which are 0.33% and 0.07% smaller than XRD results, respectively. In Fig. 3b SAED pattern was indexed according to Rhombohedral structure in line with the XRD analysis.

To find out the A-site deficiency and the B-site doping influence on the Mn covalence state and the oxygen environment in the perovskites, XPS was conducted for LSM, ALSM, LSMC5 and LSMC10. Mn spectra consist of two peaks representing Mn $2p_{1/2}$ at high binding energy and Mn $2p_{3/2}$ at low binding energy; each can be deconvoluted into three pairs of sub-peaks, for example in Mn$2p_{3/2}$, Mn^{3+} at ~640.5 eV, Mn^{4+} at ~642.5 eV and Mn* at 643.6 eV, where Mn* means Mn in mixed coordinated environment with other cations [40]. Mn^{3+} peak intensity shows obvious decrease in ALSM, LSMC5 and LSMC10 as compared to LSM, indicating Mn^{4+} and/or Mn* contents increase in these samples. Table 2 lists contents of Mn^{3+}, Mn^{4+} and Mn* calculated by peak area integration. A moderate increase of Mn^{4+} content in perovskite is vital for the surface hydroxide regeneration, one of the rate-determining steps in ORR, which is confirmed in other work [26]. This is because the increased covalence between transition metal and oxygen could increase the overlap of B-3d band and O-2*p* band, leading to the promoted charge transfer and accelerated O_2^-/OH^- displacement in ORR [26,27]. XPS of Co 2p for LSMC5 and LSMC10 in Fig. S1 is consistent with Co^{3+}, Co^{2+} and Co satellite (denoted as sat.) [41] show that Co^{3+} is the main oxidation state in both samples, with the Co^{2+} content slightly increase as x in $(La_{0.8}Sr_{0.2})_{1-x}Mn_{1-x}Co_xO_{3-\delta}$ increases. Surface Co composition of LSMC5 and LSMC10 is listed in Table S1.

XPS of O 1s for LSM, ALSM, LSMC5 and LSMC10 are displayed in

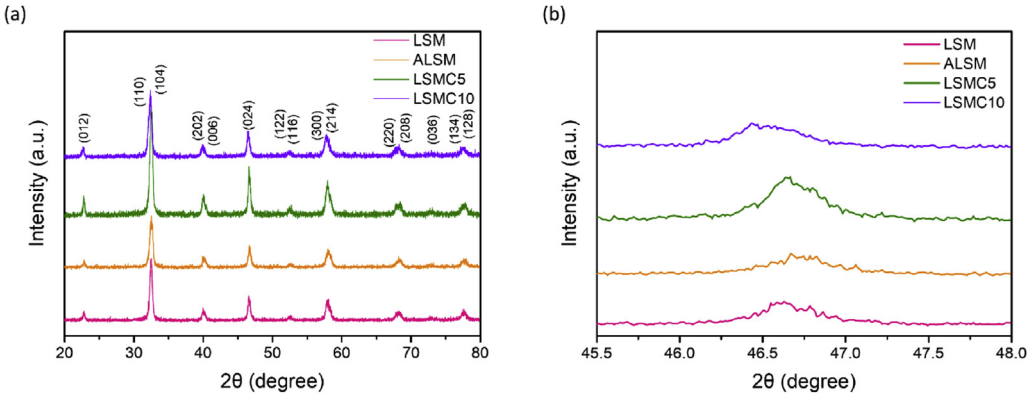

Fig. 1. (a) XRD patterns of LSM, ALSM, LSMC5 and LSMC10 perovskite catalysts and (b) Regional XRD peak shift of ALSM, LSMC5 and LSMC10 as compared with LSM.

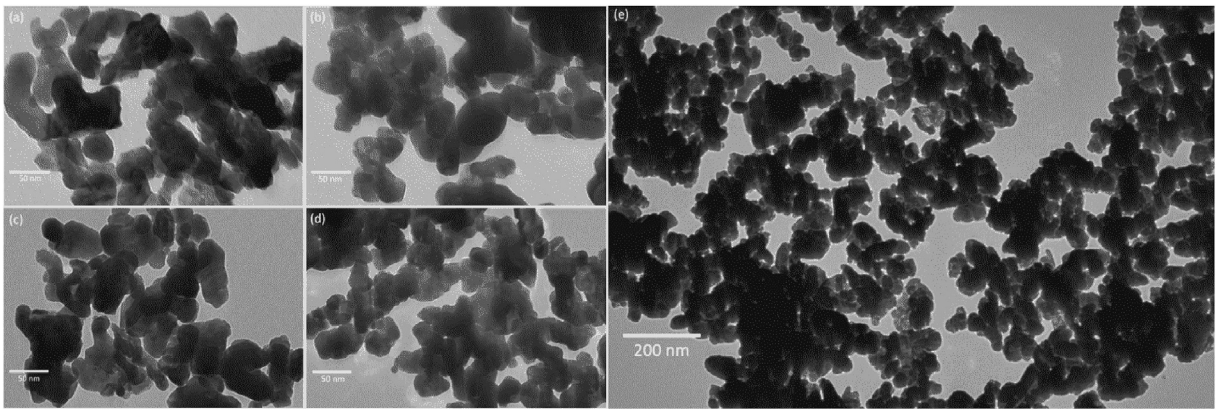

Fig. 2. TEM images of (a) LSM; (b) ALSM; (c) LSMC5; (d) LSMC10 (all 50 nm scale bar); and (e) LSM (200 nm scale bar).

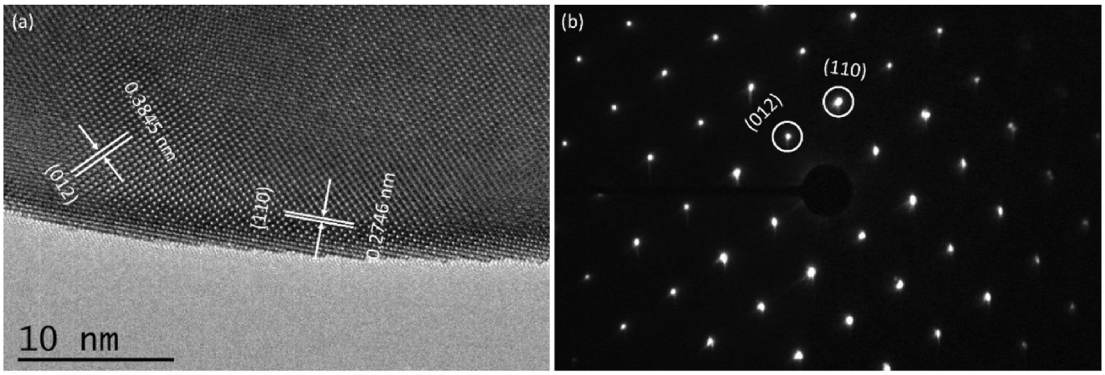

Fig. 3. (a) HRTEM and (b) SAED images of LSM.

Table 2
Mn^{3+}, Mn^{4+} and Mn* contents for LSM, ALSM, LSMC5 and LSMC10.

Samples	Mn^{3+} (%)	Mn^{4+} (%)	Mn* (%)	O^{2-} (%)	αO (%)	O_{water} (%)
LSM	30.9%	38.5%	30.6%	54.6%	20.5%	24.9%
ALSM	18.5%	57.8%	23.7%	21.1%	72.7%	6.2%
LSMC5	23.2%	48.1%	28.7%	47.9%	38.9%	13.2%
LSMC10	24.8%	44.1%	31.1%	46.2%	41.5%	12.3%

Fig. 4, apart from that of metal elements. The peak at ~529.5 eV is attributed to O^{2-} in perovskite lattice [30], and the peak at ~531.2 eV called α oxygen is related to the highly oxidative adsorbed oxygen species such as O_2^{2-}/O^- on oxygen vacancy [42,43]. The peak at ~533 eV can be assigned to physically or chemically adsorbed water [43]. In ALSM, LSMC5 and LSMC10, a dramatic increase of α oxygen content was observed, indicative of more oxygen vacancy and resulting enhanced B–O bond strength as shown in Fig. 4, which is responsible for O^{2-}/OH^- exchange, and charge transfer between surface B-site cation and oxygen adsorbates in OER [26]. Also, the oxygen vacancy could induce the increase of bulk electron density and upshift of Fermi level [44] closer to the conduction band, resulting in lower electrical resistance. The contents of oxygen species are also summarized in Table 2. It is worth noting that the charge balancing of 5% A-site deficiency in ALSM was compensated by Mn^{4+}, and mainly by oxygen vacancy according to the XPS results. In LSMC5 and LSMC10, the charge inequality is inferred to be alleviated by Co cations with enhanced hybridization with oxygen, apart from the two factors above. This hypothesis is supported by the finding that the less reducible cations in perovskite can lower the concentration of surface oxygen vacancy and preserve lattice chemical and electrochemical stability [45]. Table S2 revealed rich surface Sr and O content susceptible to be SrO-related phase on the top layers caused by electro static attraction [45]. This phenomenon is more severe for ALSM due to the B-site cation or transition metal-oxygen orbital overlap impoverishment near the surface.

To investigate the ORR catalytic ability, the catalyst ink coated on glassy carbon electrode (GCE) was tested in 0.1 M KOH solution at rotation speeds of 100, 400, 900, and 1600 rpm, respectively (Fig. S2). LSM shows high onset potential at ca. −0.09 V and therefore low overpotential compared with $La_{0.8}Sr_{0.2}MnO_3$ in other work [19,46], which can be attributed to the relatively small particle size and the consequent enhanced oxygen transfer and diffusion between the nanoparticles at early potentials [47].

Interestingly, ALSM has lower ORR performance regarding onset potential (−0.12 V) and half-wave potential (80 mV increase compared to LSM). Fig. 1a reveals lower XRD peak intensity of ALSM compared to LSM at the same heating temperature. This finding indicates that 5% A-site deficiency decreases crystallinity in ALSM, which directly influences ORR performance. Though the polarization curve implies ohmic loss characteristics, the electrochemical impedance test in OER section reveals that ALSM affords the reduced charge transfer resistance relative to LSM, suggesting that the lack of active sites could limit ORR activity that strongly depend on O_2 transfer and subsequent adsorption. For Co-doped samples, both LSMC5 and LMC10 have reduced half-wave potentials (15–20 mV decrease) but similar onset potentials as compared to LSM. This activity increase can be attributed to the fact that Mn^{4+}

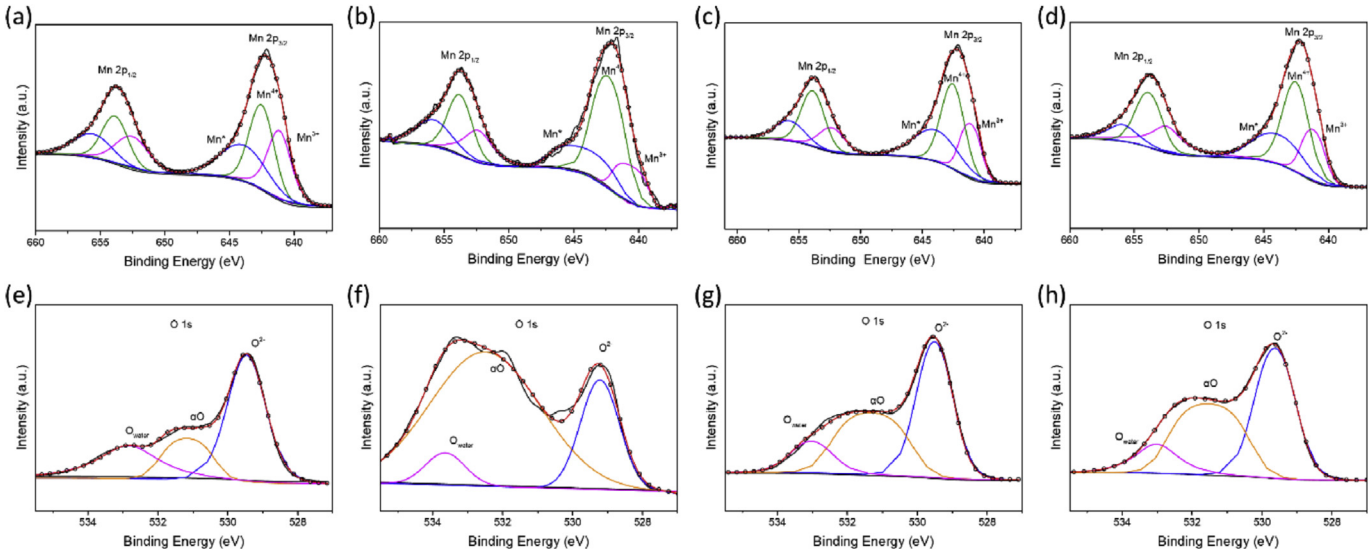

Fig. 4. Mn 2p XPS for (a) LSM, (b) ALSM, (c) LSMC5, and (d) LSMC10; O 1s XPS for (e) LSM, (f) ALSM, (g) LSMC5, and (h) LSMC10.

content (10% and 6% increase in LSMC5 and LSMC10, respectively) and the Co cation in the crystal field facilitate the orbital hybridization, which lead to a stronger metal-oxygen bond covalency and driving force for the 4th step O_2^-/OH^- exchange [26]. As discussed above, moderate amount of Mn^{4+} is essential for enhanced ORR performance, but the excessive Mn^{4+} in ALSM is accompanied by loss of oxygen and insufficient energy for O_2^- destabilization. In Fig. 5b glassy carbon has negligible ORR contribution, wherein Pt/C outperforms all samples with overpotential gap of over 100 mV at $-1.0\ mA\ cm^{-2}$.

To further study the kinetics and mass diffusion condition of ORR, Fig. 5c is the Koutecký -Levich plot (K-L plot) showing the influence of kinetic current density J_K and oxygen mass transfer controlled current density J_D on measured current density J at −0.4 V. It depicts a first-order relationship between J^{-1} and $\omega^{-1/2}$, with the electron transfer number n and extrapolated specific kinetic current density J_K plotted in Fig. 5d. ORR of LSM features a direct four-electron transfer route, but the ALSM, LSMC5 and LSMC10 have electron transfer numbers close to three, and this number decreases with increasing amounts of Co content, which is due to the decreased ORR efficiency from CoO_6 octahedra within the potential window [48]. Comparing specific kinetic current density in Fig. 5d and the Tafel plot in Fig. 5e, increased J_K and decreased Tafel slope in LSMC5 and LSMC10 were observed, reflecting superior ORR intrinsic kinetic activity and fast rate-determining step (RDS) by Co doping as the increased B–O

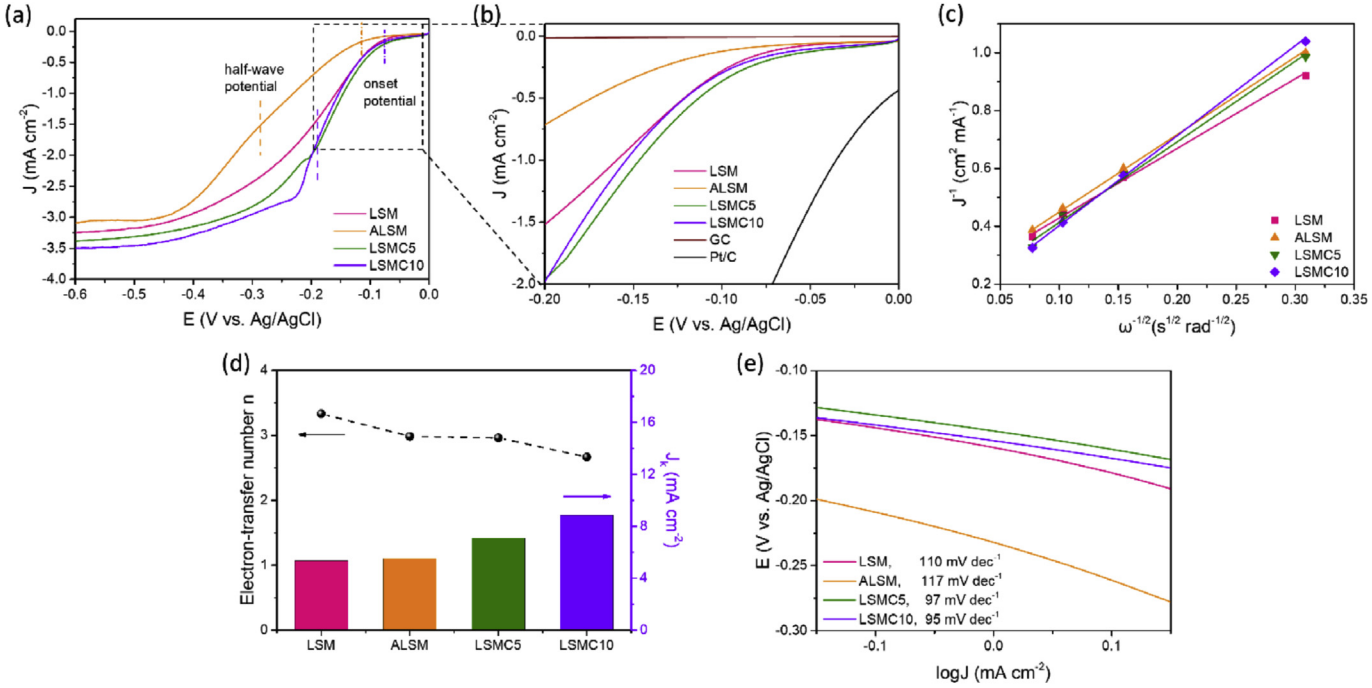

Fig. 5. (a) ORR of LSM, ALSM, LSMC5 and LSMC10 at 1600 rpm in 0.1 M KOH solution with a scan rate of 20 mV/s; (b) ORR comparison with GC electrode and Pt/C catalyst; (c) Koutecký-Levich (K–L) plots of perovskite oxides; (d) Electron transfer number n and specific kinetic current density J_K plot; and (e) Tafel plots of ORR.

hybridization can positively affect ORR [26]. Therefore, it is intriguing that doping Co can enhance ORR activity but has negative effect on ORR efficiency.

OER polarization curves of the samples were tested in 0.1 M KOH solution with a scan rate of 20 mV/s. The upper potential limit was set below 1.0 V to prevent thin film from dissolving into the solution as the O_2 bubbles strike electrode surface. $La_{0.8}Sr_{0.2}MnO_3$ itself is a weak OER catalyst relative to many other perovskite oxides, because it is inferred the structure with insufficient number of electrons in e_g antibonding orbital can hardly deprotonate oxyhydroxide groups and form peroxide ions [28]. It has been reported in several works that compared to ORR, OER measurement can better distinguish catalysts [27,29]. By introducing A-site deficiency and oxygen vacancy, ALSM outperforms LSM by 170% in OER current density at 0.8 V, even though Mn^{4+} cations are not an optimization factor for OER, as discussed above. We attribute the increase to the oxygen vacancy as it adsorbs highly oxidative oxygenated species and OH^- in alkaline media that accelerate multiple steps in an OER cycle. When doped with Co, the OER activity of LSMC5 and LSMC10 surpass that of ALSM, because the increased hybridization of six-fold Co—O structure leads to a stronger O-*2p* feature in the overlapped orbitals that enhances charge transfer between B-site cations and adsorbates [26,28,49], as well as the contribution from oxygen vacancy as discussed. From the XPS results in Table S1 and by assuming intermediate spin state for Co^{3+} and high spin state for Co^{2+}, we estimate that the Co average e_g occupation in LSMC5 and LSMC10 are 1.3 and 1.4, respectively, which are close to the optimized OER filling number ~1.2. Most notably, LSMC5 and LSMC10 outperform Pt/C catalyst in OER after 0.71 V as depicted in Fig. 6a. IrO_2 as a state-of-the-art OER catalyst reaches 5 mA cm^{-2} at ~0.60 V vs. Ag/AgCl (3.5 M) [50]. However, its relatively weak ORR performance suggests that our samples possess great potential as inexpensive noble metal-free bifunctional catalysts. Electrochemical active surface area (ECSA) measurement in Fig. 6b indicates pseudo-capacitance correlates with A-site deficiency. Normalized OER performance by mass activity and oxide surface area activity (presented by pseudo-capacity) are plotted in Fig. 6c. The oxide surface area activity suggests than LSMC10 has the highest intrinsic OER performance in spite of its low active site density. The OER results are supported by the Tafel plot in Fig. 6d. Compared to LSM, Tafel slopes of ALSM decreased by 15 mV dec^{-1}, and the slopes of LSMC5 and LSMC10 dropped by ~24 mV dec^{-1}, which suggests a change of rate-determining step from oxyhydroxide deprotonation to O—O bond formation in OOH specie [28] for the latter two catalysts.

In Fig. 6e the electrochemical impedance spectroscopy at 0.7 V with 5 mV applied voltage amplitude from 1 Hz to 10000 Hz manifests reduced resistivity in the order of ALSM, LSMC5 and LSMC10. R is resistance, C_{dl} is double-layer capacitance and Q is constant phase element. As stated before, oxygen vacancy induces the electron density increase and Fermi level upshift to the conduction band, which, together with promoted charge transfer by further overlapped Co—O orbital, facilitates OER performance. Fig. 6f shows the LSMC10 rhombohedral lattice structure with A-site deficiency and oxygen vacancy. The B-site Mn and Co cations form octahedral symmetry with O ligand by 3 d orbital splitting and overlapping with O-*2p* orbital. The atomic nonstoichiometry in the lattice can tweak the e_g orbital occupation and the σ-bonding strength with oxygenated adsorbates, which directly influence the ORR and OER activity. The design and synthesis of bifunctional perovskite catalysts should obtain the balance of oxygen vacancy, B—O orbital covalency and hybridization.

To further evaluate ORR and OER bifunctionality of the catalysts, total overpotential ΔE at which 5 mA cm^{-2} (half of the cell catalyst working current) for OER (E_{J5}) and −1 mA cm^{-2} for ORR (E_{J-1}) was calculated and summarized in Table 3. A smaller total overpotential indicates better bifunctional reactivity. The bifunctional performance of ALSM exceeds LSM due to superior OER performance.

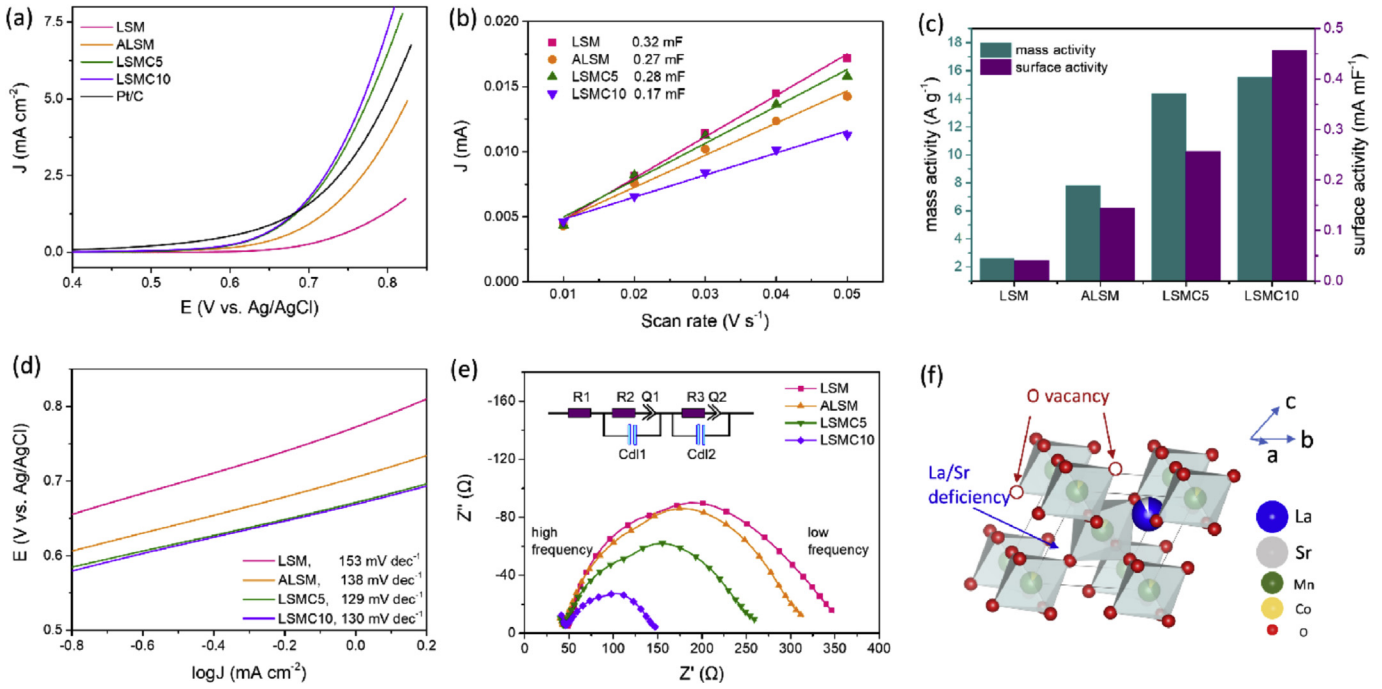

Fig. 6. (a) OER of LSM, ALSM, LSMC5, LSMC10 and Pt/C in 0.1 M KOH solution at 900 rpm rotating speed with a scan rate of 20 mV/s; (b) ECSA measurement by cyclic voltammetry (CV) from 0 to 0.1 V in non-Faradaic region. At 0.05 V, LSM has pseudo-capacity of 0.32 mF in 0.1 M KOH solution, while LSMC10 has lowest pseudo-capacity of 0.17 mF. The decreased oxide surface area proportional to pseudo-capacity correlates with A-site deficiency; (c) OER normalized by mass activity and surface activity at 0.75 V. (d) Tafel plot of perovskite oxides; (e) Electrochemical impedance spectroscopy with the inset of equivalent circuit; and (f) LSMC10 rhombohedral lattice with A-site deficiency and oxygen vacancy.

Table 3
Summary of ORR, OER onset potentials, $E_{J\text{-}1}$, E_{J5} and ΔE for catalysts.

Samples	E_{OER} onset (V)	E_{ORR} onset (V)	E_{J5} (V)	$E_{J\text{-}1}$ (V)	ΔE (V)
LSM	0.71	−0.09	–	−0.16	–
ALSM	0.69	−0.12	0.83	−0.23	1.06
LSMC5	0.67	−0.09	0.78	−0.15	0.93
LSMC10	0.67	−0.09	0.76	−0.15	0.91
Pt/C	0.68	0.05	0.80	−0.05	0.85

Table 4
Total overpotential ΔE comparison with literature.

Perovskite type	ΔE (V)	Synthesis method	Ref.
$CaCu_3Ti_4O_{12}$	~1.34	oxalate precursor route	[52]
$La_{0.8}Sr_{0.2}MnO_3$	~1.30	co-precipitation with urea	[19]
$BaMnO_3$	~1.16	mixed hydroxide synthesis	[51]
$BaTiO_{3-x}$	~1.10	acetic acid sol-gel	[29]
$La_{0.8}Sr_{0.2}Mn_{1-x}Ni_xO_3$	~1.07	citric acid-ethylene glycol sol-gel	[30]
$La_{1-x}FeO_3$	~1.04	EDTA-citric acid sol-gel	[27]
$La_{0.5}Sr_{0.5}Co_{0.8}Fe_{0.2}$	~1.00	injection chemical vapor deposition	[53]
$Ba_{0.5}Sr_{0.5}Co_xFe_{1-x}O_{3-\delta}$	~0.93	thermal reduction in Argon	[54]
$La_{0.5}Sr_{0.5}CoO_{3-x}$	~0.92	electrospinning and calcination	[55]
$(La_{0.8}Sr_{0.2})_{1-x}Mn_{1-x}Co_xO_{3-\delta}$	~0.91	PEI-EDTA PACS	this work

LSMC5 is on par with LSMC10 sharing the lowest ΔE (~0.92 V), but both carrying the disadvantage of reduced ORR efficiency. The ΔE difference between LSMC5 and LSMC10 would be more pronounced at higher applied OER voltage. Compared to perovskite catalysts prepared by precipitation, hydrothermal or conventional sol-gel-like method, the total overpotential of LSMC10 is lower than that of $La_{0.8}Sr_{0.2}MnO_3$ (~1.30 V) [19], $La_{1-x}FeO_3$ (~1.04 V) [27], $BaTiO_{3-x}$ (~1.10 V) [29], $La_{0.8}Sr_{0.2}Mn_{1-x}Ni_xO_3$ (~1.07 V) [30], $BaMnO_3$ (~1.16 V) [51], *etc*. and close to Pt/C (~0.85 V) in our test. This value is also slightly higher than that of IrO_2 (~0.86 V) according to literature [50]. Nevertheless, bifunctionality performance of LSMC10 is expected to surpass that of noble metal catalysts at higher working current densities. Detailed comparison with recent publications is listed in Table 4. Although our sample shows strong bifunctionality, its reduced electron transfer number indicates that exploration of bifunctional perovskite catalysts should work to achieve a balance between low total overpotential and high ORR efficiency.

4. Conclusions

$La_{0.8}Sr_{0.2}MnO_3$-based A-site deficiency and B-site doped perovskite catalysts were prepared by the PACS method. Nanoparticles with <100 nm size afford catalyst network which enhances oxygen diffusion and charge transfer. The A-site deficiency and the induced oxygen vacancy play a role of reduced resistivity and fast charge transfer for OER. The B-site doping method changes the hybridization of B–O orbitals and the e_g orbital filling which influence ORR and OER performance by tuning the σ-bonding strength with adsorbates. One of the lowest total overpotential in bifunctional oxygen perovskite catalysts is achieved by our LSMC10 sample owing to its small nanoparticle size, crystal defect and Co doping strategy. The rational design of bifunctional perovskite oxides for both high activity and high efficiency requires further understanding of perovskite structure and advanced techniques for nanoscale catalyst modification.

Acknowledgements

Dr. Luo thanks the support from New Mexico EPSCoR with NSF-1301346 and USDA National Institute of Food and Agriculture, HSI Collaboration: Integrating Food Science/Engineering and Education Network (IFSEEN, award number: 2015-38422-24059).

Appendix A. Supplementary data

Supplementary data related to this article can be found at https://doi.org/10.1016/j.electacta.2018.04.046.

References

[1] M.K. Debe, Electrocatalyst approaches and challenges for automotive fuel cells, Nature 486 (2012) 43–51.
[2] M. Lefèvre, E. Proietti, F. Jaouen, J.-P. Dodelet, Iron-based catalysts with improved oxygen reduction activity in polymer electrolyte fuel cells, Science 324 (2009) 71–74.
[3] M. Armand, J.-M. Tarascon, Building better batteries, Nature 451 (2008) 652–657.
[4] T. Zhang, H. Zhou, A reversible long-life lithium–air battery in ambient air, Nat. Commun. 4 (2013) 1817.
[5] S. Egelund, M. Caspersen, A. Nikiforov, P. Møller, Manufacturing of a $LaNiO_3$ composite electrode for oxygen evolution in commercial alkaline water electrolysis, Int. J. Hydrogen Energy 41 (2016) 10152–10160.
[6] J.A. Haber, Y. Cai, S. Jung, C. Xiang, S. Mitrovic, J. Jin, A.T. Bell, J.M. Gregoire, Discovering Ce-rich oxygen evolution catalysts, from high throughput screening to water electrolysis, Energy Environ. Sci. 7 (2014) 682–688.
[7] W. Zhou, J. Sunarso, Enhancing Bi-functional electrocatalytic activity of perovskite by temperature shock: a case study of $LaNiO_{3-\delta}$, J. Phys. Chem. Lett. 4 (2013) 2982–2988.
[8] M. Li, L. Zhang, Q. Xu, J. Niu, Z. Xia, N-doped graphene as catalysts for oxygen reduction and oxygen evolution reactions: theoretical considerations, J. Catal. 314 (2014) 66–72.
[9] S. Gupta, W. Kellogg, H. Xu, X. Liu, J. Cho, G. Wu, Bifunctional perovskite oxide catalysts for oxygen reduction and evolution in alkaline media, Chem. Asian J. 11 (2016) 10–21.
[10] Y. Liang, Y. Li, H. Wang, J. Zhou, J. Wang, T. Regier, H. Dai, Co_3O_4 nanocrystals on graphene as a synergistic catalyst for oxygen reduction reaction, Nat. Mater. 10 (2011) 780–786.
[11] J.-L. Shui, N.K. Karan, M. Balasubramanian, S.-Y. Li, D.-J. Liu, Fe/N/C composite in Li–O_2 battery: studies of catalytic structure and activity toward oxygen evolution reaction, J. Am. Chem. Soc. 134 (2012) 16654–16661.
[12] H.-W. Liang, W. Wei, Z.-S. Wu, X. Feng, K. Müllen, Mesoporous metal–nitrogen-doped carbon electrocatalysts for highly efficient oxygen reduction reaction, J. Am. Chem. Soc. 135 (2013) 16002–16005.
[13] M.R. Gao, J. Jiang, S.H. Yu, Solution-based synthesis and design of late transition metal chalcogenide materials for oxygen reduction reaction (ORR), Small 8 (2012) 13–27.
[14] H. Wang, Y. Liang, Y. Li, H. Dai, $Co_{1-x}S$–graphene hybrid: a high-performance metal chalcogenide electrocatalyst for oxygen reduction, Angew. Chem. Int. Ed. 50 (2011) 10969–10972.
[15] K. Gong, F. Du, Z. Xia, M. Durstock, L. Dai, Nitrogen-doped carbon nanotube arrays with high electrocatalytic activity for oxygen reduction, Science 323 (2009) 760–764.
[16] H.T. Chung, J.H. Won, P. Zelenay, Active and stable carbon nanotube/nanoparticle composite electrocatalyst for oxygen reduction, Nat. Commun. 4 (2013) 1922.
[17] D.H. Lee, W.J. Lee, W.J. Lee, S.O. Kim, Y.-H. Kim, Theory, synthesis, and oxygen reduction catalysis of Fe-porphyrin-like carbon nanotube, Phys. Rev. Lett. 106 (2011), 175502.
[18] Y. Zhao, L. Xu, L. Mai, C. Han, Q. An, X. Xu, X. Liu, Q. Zhang, Hierarchical mesoporous perovskite $La_{0.5}Sr_{0.5}CoO_{2.91}$ nanowires with ultrahigh capacity for Li-air batteries, Proc. Natl. Acad. Sci. U.S.A. 109 (2012) 19569–19574.
[19] C. Jin, X. Cao, L. Zhang, C. Zhang, R. Yang, Preparation and electrochemical properties of urchin-like $La_{0.8}Sr_{0.2}MnO_3$ perovskite oxide as a bifunctional catalyst for oxygen reduction and oxygen evolution reaction, J. Power Sources 241 (2013) 225–230.
[20] J.I. Jung, H.Y. Jeong, J.S. Lee, M.G. Kim, J. Cho, A bifunctional perovskite catalyst for oxygen reduction and evolution, Angew. Chem. Int. Ed. 53 (2014) 4582–4586.
[21] R. Liu, Y. Wang, D. Liu, Y. Zou, S. Wang, Water-plasma-enabled exfoliation of ultrathin layered double hydroxide nanosheets with multivacancies for water oxidation, Adv. Mater. 29 (2017), 1701546.
[22] Y. Wang, Y. Zhang, Z. Liu, C. Xie, S. Feng, D. Liu, M. Shao, S. Wang, Layered double hydroxide nanosheets with multiple vacancies obtained by dry exfoliation as highly efficient oxygen evolution electrocatalysts, Angew. Chem. Int. Ed. 56 (2017) 5867–5871.
[23] Y. Wang, C. Xie, Z. Zhang, D. Liu, R. Chen, S. Wang, In situ exfoliated, N-Doped, and edge-rich ultrathin layered double hydroxides nanosheets for oxygen evolution reaction, Adv. Funct. Mater. 28 (2018), 1703363.
[24] Y. Wang, L. Tao, Z. Xiao, R. Chen, Z. Jiang, S. Wang, 3D carbon electrocatalysts in situ constructed by defect-rich nanosheets and polyhedrons from NaCl-sealed zeolitic imidazolate frameworks, Adv. Funct. Mater. 28 (2018), 1705356.

[25] G. Li, K. Zhang, M.A. Mezaal, L. Lei, Synthesis and electrochemical evaluation of $La_{1-x}Sr_xMnO_3$ catalysts for zinc-air batteries, J. Solid State Electrochem. 20 (2016) 421–427.
[26] J. Suntivich, H.A. Gasteiger, N. Yabuuchi, H. Nakanishi, J.B. Goodenough, Y. Shao-Horn, Design principles for oxygen-reduction activity on perovskite oxide catalysts for fuel cells and metal–air batteries, Nat. Chem. 3 (2011) 546–550.
[27] Y. Zhu, W. Zhou, J. Yu, Y. Chen, M. Liu, Z. Shao, Enhancing electrocatalytic activity of perovskite oxides by tuning cation deficiency for oxygen reduction and evolution reactions, Chem. Mater. 28 (2016) 1691–1697.
[28] J. Suntivich, K.J. May, H.A. Gasteiger, J.B. Goodenough, Y. Shao-Horn, A perovskite oxide optimized for oxygen evolution catalysis from molecular orbital principles, Science 334 (2011) 1383–1385.
[29] C.-F. Chen, G. King, R.M. Dickerson, P.A. Papin, S. Gupta, W.R. Kellogg, G. Wu, Oxygen-deficient $BaTiO_{3-x}$ perovskite as an efficient bifunctional oxygen electrocatalyst, Nano Energy 13 (2015) 423–432.
[30] Z. Wang, Y. You, J. Yuan, Y.-X. Yin, Y.-T. Li, S. Xin, D. Zhang, Nickel-doped $La_{0.8}Sr_{0.2}Mn_{1-x}Ni_xO_3$ nanoparticles containing abundant oxygen vacancies as an optimized bifunctional catalyst for oxygen cathode in rechargeable lithium–air batteries, ACS Appl. Mater. Interfaces 8 (2016) 6520–6528.
[31] K.J. May, C.E. Carlton, K.A. Stoerzinger, M. Risch, J. Suntivich, Y.-L. Lee, A. Grimaud, Y. Shao-Horn, Influence of oxygen evolution during water oxidation on the surface of perovskite oxide catalysts, J. Phys. Chem. Lett. 3 (2012) 3264–3270.
[32] H. Luo, A.H. Mueller, T.M. McCleskey, A.K. Burrell, E. Bauer, Q. Jia, Structural and photoelectrochemical properties of $BiVO_4$ thin films, J. Phys. Chem. C 112 (2008) 6099–6102.
[33] Q. Yi, H. Wang, S. Cong, Y. Cao, Y. Wang, Y. Sun, Y. Lou, J. Zhao, J. Wu, G. Zou, Self-cleaning glass of photocatalytic anatase TiO_2@ carbon nanotubes thin film by polymer-assisted approach, Nanoscale Res. Lett. 11 (2016) 457.
[34] L. Fei, H.K. Reddy, J. Hill, Q. Lin, B. Yuan, Y. Xu, P. Dailey, S. Deng, H. Luo, Preparation of mesoporous silica-supported palladium catalysts for biofuel upgrade, J. Nanotechnol. 2012 (2012) 6.
[35] W. Li, J. Wang, H. Huang, W. Qiao, D. Long, L. Ling, Polymer-assisted synthesis of nanoparticle Co_3O_4/CeO_2 catalyst for carbon monoxide low-temperature oxidation, Acta Sci. Circumstantiae 36 (2016) 294–300.
[36] O. Lori, S. Gonen, L. Elbaz, Highly active, corrosion-resistant cathode for fuel cells, based on platinum and molybdenum carbide, J. Electrochem. Soc. 164 (2017) F825–F830.
[37] A.K. Burrell, T.M. McCleskey, Q. Jia, Polymer assisted deposition, ChemComm (2008) 1271–1277.
[38] B. Nagabhushana, R.S. Chakradhar, K. Ramesh, C. Shivakumara, G. Chandrappa, Low temperature synthesis, structural characterization, and zero-field resistivity of nanocrystalline $La_{1-x}Sr_xMnO_{3+\delta}$($0.0 \leq x \leq 0.3$) manganites, Mater. Res. Bull. 41 (2006) 1735–1746.
[39] Q. Jia, T.M. McCleskey, A. Burrell, Y. Lin, G. Collis, H. Wang, A. Li, S. Foltyn, Polymer-assisted deposition of metal-oxide films, Nat. Mater. 3 (2004) 529–532.
[40] A. Giri, N. Goswami, M. Bootharaju, P.L. Xavier, R. John, N.T. Thanh, T. Pradeep, B. Ghosh, A. Raychaudhuri, S.K. Pal, Emergence of multicolor photoluminescence in $La_{0.67}Sr_{0.33}MnO_3$ nanoparticles, J. Phys. Chem. C 116 (2012) 25623–25629.
[41] Y. Zhu, W. Zhou, Z.G. Chen, Y. Chen, C. Su, M.O. Tadé, Z. Shao, $SrNb_{0.1}Co_{0.7}Fe_{0.2}O_{3-\delta}$ perovskite as a next-generation electrocatalyst for oxygen evolution in alkaline solution, Angew. Chem. Int. Ed. 54 (2015) 3897–3901.
[42] J. Hu, L. Wang, L. Shi, H. Huang, Oxygen reduction reaction activity of $LaMn_{1-x}Co_xO_3$-graphene nanocomposite for zinc-air battery, Electrochim. Acta 161 (2015) 115–123.
[43] S. Mickevičius, S. Grebinskij, V. Bondarenka, B. Vengalis, K. Šliužienė, B. Orlowski, V. Osinniy, W. Drube, Investigation of epitaxial $LaNiO_{3-x}$ thin films by high-energy XPS, J. Alloy. Comp. 423 (2006) 107–111.
[44] W.T. Hong, M. Risch, K.A. Stoerzinger, A. Grimaud, J. Suntivich, Y. Shao-Horn, Toward the rational design of non-precious transition metal oxides for oxygen electrocatalysis, Energy Environ. Sci. 8 (2015) 1404–1427.
[45] N. Tsvetkov, Q. Lu, L. Sun, E.J. Crumlin, B. Yildiz, Improved chemical and electrochemical stability of perovskite oxides with less reducible cations at the surface, Nat. Mater. 15 (2016) 1010–1016.
[46] F. Lu, J. Sui, J. Su, C. Jin, M. Shen, R. Yang, Hollow spherical $La_{0.8}Sr_{0.2}MnO_3$ perovskite oxide with enhanced catalytic activities for the oxygen reduction reaction, J. Power Sources 271 (2014) 55–59.
[47] L. Yan, Y. Lin, X. Yu, W. Xu, T. Salas, H. Smallidge, M. Zhou, H. Luo, $La_{0.8}Sr_{0.2}MnO_3$-Based perovskite nanoparticles with the a-site deficiency as high performance bifunctional oxygen catalyst in alkaline solution, ACS Appl. Mater. Interfaces 9 (2017) 23820–23827.
[48] J. Sunarso, A.A. Torriero, W. Zhou, P.C. Howlett, M. Forsyth, Oxygen reduction reaction activity of La-based perovskite oxides in alkaline medium: a thin-film rotating ring-disk electrode study, J. Phys. Chem. C 116 (2012) 5827–5834.
[49] K. Lopez, G. Park, H.-J. Sun, J.-C. An, S. Eom, J. Shim, Electrochemical characterizations of $LaMO_3$ (M= Co, Mn, Fe, and Ni) and partially substituted $LaNi_xM_{1-x}O_3$ (x= 0.25 or 0.5) for oxygen reduction and evolution in alkaline solution, J. Appl. Electrochem. 45 (2015) 313–323.
[50] Y. Zhao, K. Kamiya, K. Hashimoto, S. Nakanishi, Efficient bifunctional Fe/C/N electrocatalysts for oxygen reduction and evolution reaction, J. Phys. Chem. C 119 (2015) 2583–2588.
[51] Y. Xu, A. Tsou, Y. Fu, J. Wang, J.-H. Tian, R. Yang, Carbon-coated perovskite $BaMnO_3$ porous nanorods with enhanced electrocatalytic perporites for oxygen reduction and oxygen evolution, Electrochim. Acta 174 (2015) 551–556.
[52] H. Kushwaha, A. Halder, P. Thomas, R. Vaish, $CaCu_3Ti_4O_{12}$: a bifunctional perovskite electrocatalyst for oxygen evolution and reduction reaction in alkaline medium, Electrochim. Acta 252 (2017) 532–540.
[53] H.W. Park, D.U. Lee, M.G. Park, R. Ahmed, M.H. Seo, L.F. Nazar, Z. Chen, Perovskite–nitrogen-doped carbon nanotube composite as bifunctional catalysts for rechargeable lithium–air batteries, ChemSusChem 8 (2015) 1058–1065.
[54] J.I. Jung, S. Park, M.G. Kim, J. Cho, Tunable internal and surface structures of the bifunctional oxygen perovskite catalysts, Adv. Energy Mater. 5 (2015) 13.
[55] G. Liu, H. Chen, L. Xia, S. Wang, L.-X. Ding, D. Li, K. Xiao, S. Dai, H. Wang, Hierarchical mesoporous/macroporous perovskite $La_{0.5}Sr_{0.5}CoO_{3-x}$ nanotubes: a bifunctional catalyst with enhanced activity and cycle stability for rechargeable lithium oxygen batteries, ACS Appl. Mater. Interfaces 7 (2015) 22478–22486.